Inorganic Chemistry
Article
pubs.acs.org/IC

3c/4e $\hat{\sigma}$-Type Long-Bonding: A Novel Transitional Motif toward the Metallic Delocalization Limit

C. R. Landis* and F. Weinhold

Department of Chemistry, University of Wisconsin, Madison, Wisconsin 53706, United States

Supporting Information

ABSTRACT: We describe a novel "long-bonding" motif that appears in the framework of natural bond orbital (NBO) analysis as a surprising form of 3-center, 4-electron (3c/4e) L···A···L′ bonding with "inverted" electronegativity pattern $\Xi_A > \Xi_L, \Xi_L{}'$. Such long-bonding (denoted L^L′) underlies the predicted (meta)stability of exotic rare gas species with highly electronegative ligands (e.g., HeF_2, NeF_2) as well as the *absolute* stability of low-electronegativity metallic triads (e.g., $BeLi_2$, $ZnCu_2$, and related species) that are experimentally unknown but can be anticipated from simple valency and electronegativity trends. We focus particularly on the $BeLi_2$ triad, whose Lewis-type Li^Li′ long bond is of paradoxical *anti*bonding phase pattern, denoted $\hat{\sigma}^*{}_{LiLi'}$ to suggest its essential $2^{-1/2}(s_{Li} - s_{Li'})$ orbital composition. We demonstrate how the long-bonded triad serves as a fundamental building-block for numerous 1-, 2-, and 3-d structures that are predicted to exhibit extraordinary calorimetric, vibrational, and electric polarizability properties, commonly associated with the delocalized metallic limit. Both thermodynamic and kinetic results support the NBO inference that $\hat{\sigma}/\hat{\sigma}^*$-type long-bonding signals the transition to a fundamentally new regime of chemical association, separated by significant activation barriers from the covalent molecular domain and characterized by *reversed* perturbative precedence of Lewis-type vs resonance-type donor−acceptor contributions. Long-bond resonance therefore appears to be of central importance to a broadened conceptual picture of molecular and metallic interaction phenomena.

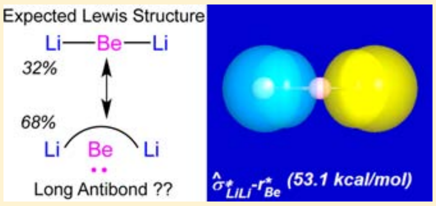

I. INTRODUCTION

The well-known 3-center/2-electron hypovalent (3c/2e; bridging τ-type) and 3-center/4-electron hypervalent (3c/4e; Pimentel-Rundle-Coulson ω-type) bonding motifs[1] constitute the best known exceptions to the chemist's standard Lewis-structural model. Such 3c motifs are but the first steps leading from localized (1c,2c) covalent bonding to the delocalized multicenter binding of the metallic limit, commonly associated with "free electron," "jellium," and Bloch-type models of solid state physics.[2] In the present work, we employ natural bond orbital (NBO) analysis[3] of ab initio and density functional theory (DFT) wave functions to identify a distinctive "inverted electronegativity" variant of 3c/4e bonding that is predicted to yield highly unusual chemical species (e.g., HeF_2, $BeLi_2$) with properties suggestive of transitional character between idealized "molecular" and "metallic" bonding regimes.

NBO analysis is a particularly effective tool[4] for uncovering localized bonding patterns intermediate between the idealized limits of 2c covalency and free-electron ("∞c") behavior. Rather than constituents of a preconceived bonding model, NBOs are the algorithmic result of systematic search for localized few-center functional forms that optimally describe the electron density of a given (approximate or exact) solution of the Schrödinger equation. The chosen theoretical description may correspond to any desired DFT or wave function approximation (correlated or uncorrelated, variational or perturbative)[5] that adequately describes the species of interest. The determinantal wave function Ψ_L of high-occupancy Lewis-type (L-type "donor") NBOs forms the natural Lewis structure (NLS) starting point for resonance-type perturbative corrections associated with partial occupancy of non-Lewis (NL-type "acceptor") NBOs. Natural resonance theory (NRT)[6] further quantifies such donor−acceptor corrections in terms of the relative weightings of NLS and other contributing resonance structures, as well as associated NRT bond orders $\{b_{AB}\}$ for each A-B atom pair of the resonance hybrid. Unless otherwise stated, in the present work we employ standard B3LYP/6-311++G** level of DFT, which offers considerable computational efficiency and allows second-order perturbative estimates $\Delta E^{(2)}{}_{D\to A}$ of NBO donor−acceptor interaction energy[7] to be evaluated from the Kohn−Sham effective 1e-Hamiltonian operator.[8]

Considerable controversy surrounds the characterization of "metallic bonding." For binary A/B compounds, the relationship of metallicity (M) to covalent (C) and ionic (I) A-B character is often depicted in bonding triangles (*Dreieckeschema*)[9] with idealized (M,C,I) vertex limits. The qualitative van Arkel triangle and related equilateral forms[10] can be expressed more quantitatively[11] in terms of average and difference values of atomic electronegativity,

$$\Xi_{av} = (\Xi_A + \Xi_B)/2 \tag{1}$$

$$\delta\Xi = |\Xi_A - \Xi_B| \tag{2}$$

Received: January 7, 2013
Published: April 18, 2013

© 2013 American Chemical Society

The usefulness of such diagrams suggests an association of metallicity with reduced electronegativity difference and reduced ionicity, particularly in systems of low Ξ_{av}. However, these insights refer only to two-center A-B properties, and thus provide little guidance to expected *multi*-center wave function character as metallicity increases, even in elemental or binary systems. For isolated metal atoms embedded in a molecular or coordinative environment of organic ligands, it is usually possible to formulate a satisfactory localized Lewis-like bonding picture[12] that bears many parallels to those commonly known for nonmetallic species. Nevertheless, as bulk metallic character increases, for example, in large metal atom clusters[13] or true metallic phases,[14] the chemist's localized bonding models tend to falter or fail,[15] and primary theoretical focus turns from bonding concepts of the chemist to the free electron-type models of solid-state physics.[16] Indeed, an unresolved question is whether the "metallic bond" exists at all.[17]

An outline of our work is as follows: In Sec. II we review the NBO/NRT formulation of ω-type hyperbonding (as exemplified in FHF^-, F_3^-, and other species) in the framework of the general Pimentel–Rundle–Coulson 3-center molecular orbital (MO) model.[18] This allows us to recognize the mathematical possibility of a strange *long-bond* ("$\hat{\sigma}$-type") resonance form that is found to achieve significant NRT weighting even in classical ω-bonded species such as F_3^-, and becomes *dominant* in isoelectronic NeF_2 and other surprising main-group and transition metal triatomics. In Sec. III we investigate the potential energy surface of the prototypical $\hat{\sigma}^*$-bonded $BeLi_2$ triad, including its thermodynamic and kinetic stability with respect to corresponding σ-bonded species, its propensity for higher-order clustering in 1, 2, and 3 dimensions, and its distinctive structural, electrical, and spectroscopic properties that suggest a connection to limiting "metallic" delocalization.[19] Sec. IV offers a summary and final conclusions.

II. THREE-CENTER, FOUR-ELECTRON HYPERBONDING IN METALLIC AND NON-METALLIC ATOMIC TRIADS

3c/4e hypervalency is usually viewed as a form of dative (Lewis acid–base) interaction in which a coordinating ligand (L:) competes with an existing coordinative bond (A:L′) involving equivalent or near-equivalent lone pair-bearing ligand L′:, leading to near-degenerate dissociative pathways, namely,

$$\begin{tikzcd}[row sep=small] & \underset{\mathbf{I}}{\mathrm{L{:}\ +\ A{:}L'}} \\ \mathrm{L{:}\cdots A\cdots{:}L'} \arrow[ur] \arrow[dr] & \\ & \underset{\mathbf{II}}{\mathrm{L{:}A\ +\ {:}L'}} \end{tikzcd} \qquad (3)$$

The intact molecular species on the left appears to have "too many electrons" to be viewed as a conventional Lewis structure, whereas dissociated forms **I**, **II** are unexceptional. As recognized by Coulson,[18c] the alternative formulations on the right of (3) can be regarded as intermolecular resonance structures that contribute (near-)equal weightings w_I, w_{II} and approximate *half*-bonds to the resonance hybrid on the left, namely,

$$w_{I} \cong w_{II} \qquad (4a)$$

$$b_{AL} \cong b_{AL'} \cong 1/2, \qquad b_{LL'} \cong 0 \qquad (4b)$$

As emphasized by Herzberg,[20] the resonance *is* the binding.

Because the resonance mixing in (3) involves three atomic centers competing for two electron pairs, it is also described as "three-center, four-electron (3c/4e) hypervalency." The phenomenon can also be identified as "hyperbonding" and denoted by a distinctive stroke-symbol ($\mathrm{L}\vdash\mathrm{A}\dashv\mathrm{L'}$) and ω-bond notation[1] that suggests its unique electronic character, namely,

$$\omega_{LA:L'} \leftrightarrow \text{2c/2e } \mathrm{L}\vdash\mathrm{A} \text{ bond, with proximal :L}' \text{ ligand} \qquad (5a)$$

$$\omega_{L:AL'} \leftrightarrow \text{2c/2e } \mathrm{A}\dashv\mathrm{L'} \text{ bond, with proximal :L ligand} \qquad (5b)$$

$$\omega_{LAL'} \leftrightarrow \text{3c/4e } \mathrm{L}\vdash\mathrm{A}\dashv\mathrm{L'}\ \textit{hyper}\text{bond [resonance hybrid of (5a,b)]} \qquad (5c)$$

Deeper mathematical aspects of hyperbonded 3c/4e species can be discussed in alternative molecular orbital[18a,21] or valence bond[22] formulations, but the resonance-hybrid formulation (3) seems to capture the essence of ω-bonding most succinctly and intuitively.

In exceptional cases, a stranger resonance form of 3c/4e interaction, *long*-bonding, may become dominant, as depicted schematically in (6):

$$\mathrm{L\cdots A\cdots L'} \leftrightarrow \underset{\mathbf{III}}{\widehat{\mathrm{L\ \ddot{A}\ L'}}} \qquad (6)$$

In this case, the 2-center electron pair of (6) is found to be shared between the *terminal* L, L′ atoms, constituting a valid L-L′ (or L^L′) "shared electron pair" in the Lewis sense, even though these atoms are spatially *separated* by the central A atom! Correspondingly, the NRT weightings and bond orders contrast sharply with those in (4a,b),

$$w_{III} \cong 1 \qquad (7a)$$

$$b_{LL'} \cong 1, \qquad b_{AL} \cong b_{AL'} \cong 0 \qquad (7b)$$

We denote the 2c/2e long-bond of (6) by a caret ("hat")-shaped connector over the bonded atoms in a Lewis-like structure diagram, and we place a caret accent over the usual bond symbol ($\hat{\sigma}$,$\hat{\sigma}^*$, etc.) to label such $\hat{\sigma}$-type long-bonds and the distinctive $\hat{\sigma}$-bonding electronic motif. The ω-bonding limit (3) has been widely recognized and characterized in molecular orbital[21] and valence bond[22] terms, but the broader importance of the $\hat{\sigma}$-type long-bonding limit of 3c/4e hypervalency seems not to have been sufficiently appreciated.

The $\hat{\sigma}$-bonded structure **III** appears chemically reasonable if the three atoms are in approximate equilateral triangular geometry, where resonance structures **I**, **II**, and **III** become equivalent. But even at the limit of linear or near-linear L-A-L′ geometry, structure **III** remains a mathematical possibility whose resonance weighting w_{III} can be calculated from an accurate wave function. Thus, the likelihood or unlikelihood of 3c/4e ω-bonding (3) vs $\hat{\sigma}$-bonding (6) remains to be determined through NRT analysis of specific chemical systems.

What are the chemical factors expected to drive a chemical species toward ω-bonding vs $\hat{\sigma}$-bonding in a given 3-center region? The principal stabilizations associated with each bonding pattern are revealed by NBO analysis of donor–acceptor interactions that the pattern makes available. For the ω-bonded pattern (3), the available valence-shell donors and acceptors are, respectively, the n_L ($n_{L'}$) lone pairs and $\sigma^*_{AL'}$ (σ^*_{AL}) valence antibonds, leading to corresponding NBO stabilizations

$$n_L \rightarrow \sigma^*_{AL'}(\mathbf{I}) \qquad (8a)$$

$$n_{L'} \rightarrow \sigma^*_{AL}(\mathbf{II}) \qquad (8b)$$

For the $\hat{\sigma}$-bonded pattern (6), the leading donor is the central n_A lone pair and the corresponding acceptor is the non-Lewis $\hat{\sigma}$-type $\hat{\sigma}^{(NL)}_{LL'}$, leading to NBO stabilization

Table 1. Hyperbonded Linear Triatomics L-A-L′, Showing Atomic Binding Energy (ΔE_{bind}, kcal/mol), Equilibrium Bond Length (R_{AL}, Å), NPA Atomic Charges (Q_A, Q_L), NRT Weightings ($w_{\text{I//II//III}}$, %) and Central Atomic Valency (V_A), Leading Donor−Acceptor Stabilization ($\Delta E^{(2)}{}_{\text{D}\rightarrow\text{A}}$, kcal/mol), and Dominant Hyperbond Type ($\omega/\hat{\sigma}/\hat{\sigma}^*$) for Each Species

L-A-L′	ΔE_{bind}	R_{AL}	Q_A	Q_L	$w_{\text{I/II}}$	w_{III}	V_A	$\Delta E^{(2)}{}_{\text{D}\rightarrow\text{A}}$	type
F−F−F$^-$	−69.7	1.745	−0.107	−0.446	43.6	12.9	0.872	133.8	ω
F−Ne−F	+69.0	1.874	+0.228	−0.114	13.1	73.7	0.262	57.1	$\hat{\sigma}$
F−He−F	+38.9	1.246	+0.515	−0.257	23.6	52.8	0.472	421.1	$\hat{\sigma}^*$
F−Ar−F	+13.8	1.878	+0.756	−0.378	41.6	16.9	0.338	169.9	ω
Li−Li−Li$^-$	−40.7	3.011	+0.026	−0.513	43.2	13.6	0.864	27.0	ω
Li−Be−Li	−36.7	2.504	−0.006	+0.003	19.2	61.7	0.384	55.7	$\hat{\sigma}^*$
Cu−Cu−Cu$^-$	−81.4	2.383	−0.014	−0.493	41.7	16.7	0.834	81.9	ω
Cu−Zn−Cu	−50.1	2.350	+0.228	−0.114	29.8	40.5	0.596	114.7	$\hat{\sigma}^*$

$$n_A \rightarrow \hat{\sigma}^{(NL)}_{LL'}(\mathbf{III}) \tag{9}$$

where $\hat{\sigma}^{(NL)}{}_{LL'}$ might be either $\hat{\sigma}_{LL'}$ or $\hat{\sigma}^*{}_{LL'}$, the orthogonally paired mixtures of in-phase and out-of-phase bonding hybrids h_L, $h_{L'}$,

$$\hat{\sigma}_{LL'} = c_L h_L + c_{L'} h_{L'} \tag{10a}$$

$$\hat{\sigma}^*{}_{LL'} = c_{L'} h_L - c_L h_{L'} \tag{10b}$$

Although it seems evident that the *in*-phase combination (with $c_L \cong c_{L'} \cong 2^{-1/2}$) must be preferred as the occupied Lewis-type $\hat{\sigma}^{(L)}{}_{LL'}$ if hybrids h_L, $h_{L'}$ have strong positive overlap, this phase pattern is no longer obligatory in the long-range $\hat{\sigma}$-bonding limit where in-phase and out-of-phase h_L-$h_{L'}$ mixing combinations become energetically degenerate. Rather, the preferred $\hat{\sigma}^{(L)}{}_{LL'}$ phase pattern will be dictated by the symmetry of the *donor* n_A orbital in (9) and its favorable mixing with the non-Lewis *acceptor* $\hat{\sigma}^{(NL)}{}_{LL'}$orbital of suitable form.

For main-group A atoms, n_A must be of predominant s or p type to maintain the symmetry of bonding interactions with opposite directions. The s_A-type donor lone pair is therefore expected to demand the *in*-phase $\hat{\sigma}^{(NL)}{}_{LL'}$ combination as non-Lewis acceptor,

$$\hat{\sigma}^{(NL)}_{LL'} = \hat{\sigma}_{LL'}, \quad \text{if } n_A = s_A\text{-type} \tag{11a}$$

so that both h_L, $h_{L'}$ can overlap the all-positive outer lobe of s_A. In contrast, the p_A-type donor lone pair demands the *out*-of-phase $\hat{\sigma}^{(NL)}{}_{LL'}$ combination as acceptor,

$$\hat{\sigma}^{(NL)}_{LL'} = \hat{\sigma}^*{}_{LL'}, \quad \text{if } n_A = p_A\text{-type} \tag{11b}$$

so that h_L, $h_{L'}$ both have in-phase overlap with the *opposite* lobes of p_A. However, the former case dictates that the occupied Lewis-type $\hat{\sigma}_{LL'}$ bond is the *out*-of-phase ("antibonding" $\hat{\sigma}^*$) combination.[23] The paradoxical phase-pattern of occupied NBOs in the case of an s_A-type central donor orbital emphasizes that the "2-center" electron-sharing of the ligand hybrids is dictated by their shared 3c/4e coherence with the central n_A orbital, rather than the usual direct h_L, $h_{L'}$ overlap of conventional 2c/2e bonding.

Electronegativity patterns in the L-A-L′ triad are also expected to affect ω- vs $\hat{\sigma}$-bonding propensity.[22] The ω-bonding interactions (8a,b) are evidently maximized for ionic or highly polar triads in which the electronegativity of central atom A is *less* than that of terminal L, L′,

$$\Xi_A < \Xi_L, \Xi_{L'} \quad (\text{favors } \mathbf{I, II}) \tag{12a}$$

thereby polarizing both $\sigma^*{}_{AL}$, $\sigma^*{}_{AL'}$ toward the A-end of the antibond to strengthen its interaction with the adjacent lone pair, as depicted in resonance forms **I**, **II**. In contrast, the $\hat{\sigma}$-bonding interaction is expected to be enhanced for neutral or relatively apolar triads that exhibit the *inverse* electronegativity pattern

$$\Xi_A > \Xi_L, \Xi_{L'} \quad (\text{favors } \mathbf{III}) \tag{12b}$$

which promotes retention of 1c nonbonding character at A and 2c release (donation/sharing) at L, L′, as depicted in resonance form **III**.

From the above considerations, we can anticipate that (9) is written more specifically as

$$n_A \rightarrow \hat{\sigma}_{LL'} \cong 2^{-1/2}(h_L + h_{L'}), \quad \text{if } n_A = s_A\text{-type} \tag{13a}$$

$$n_A \rightarrow \hat{\sigma}^*{}_{LL'} \cong 2^{-1/2}(h_L - h_{L'}), \quad \text{if } n_A = p_A\text{-type} \tag{13b}$$

Furthermore, we expect that $\hat{\sigma}$-type bonding (6) is favored if the central Ä is relatively *un*suited to directional sigma-bonding, tending instead toward nonbonding character in neutral triads with relatively electropositive monovalent ligands L, L′, consistent with the inverse-electronegativity pattern (12b). The inverted electronegativities, weakened directional-bonding propensity, and electronic delocalization associated with resonance pattern (9) are all suggestive of the metallic bonding limit. We may therefore anticipate a more general association of $\hat{\sigma}$-bonding with distinctive metal-like properties of the 3c/4e triad, as will be illustrated in examples below.

Secondary Long-Bonding in Trifluoride Anion. The puzzles presented by main-group hypervalent 3c/4e species are exemplified by familiar trihalide anions such as F_3^-, Cl_3^-, or I_3^-. Because F_3^- has 22 valence electrons, it has "too many" electrons to form the octets of a conventional Lewis dot diagram. Nevertheless, the F_3^- anion is bound by ~38 kcal/mol with respect to $F^- + F_2$ dissociation, showing that 3c/4e ω-bonding can be surprisingly robust compared to ordinary 2c/2e covalent σ-bonding (cf. 31.7 kcal/mol for the σ-bond of F_2).

To investigate the resonance weightings in F_3^-, we employ NRT analysis with all three resonance structures **I**, **II**, **III** specified as reference structures to ensure balanced numerical treatment even if a particular structure falls below the default reference threshold. In this case, the two ω-bonded structures (RS 1,2) and $\hat{\sigma}$-bonded structure (RS 3) are found to constitute 100% of the NRT expansion,

$$w_{\mathbf{I}} = w_{\mathbf{II}} = 43.6\%, \quad w_{\mathbf{III}} = 12.9\% \tag{14}$$

so the NRT bond orders and valencies are related rather trivially to the resonance weightings, as shown in the first row of Table 1. We note that BOVB (breathing orbital valence bond) calculations of Braida and Hiberty[22] yield reasonably similar resonance weightings ($w_{\mathbf{I}} = w_{\mathbf{II}} = 37\%$, $w_{\mathbf{III}} = 26\%$, when corrected for ionic-covalent vs Coulson−Fischer representations) despite the very different wave function methods.

As anticipated (4a and 4b), the two ω-bond weightings (RS 1,2) contribute approximately half-bond order ($b_{12} = b_{13} = 0.436$) to the F(1)−F(2) and F(1)−F(3) members of the 3c/4e triad. But it is also striking that $\hat{\sigma}$-bond weighting (RS 3) contributes appreciable F(2)−F(3) *long*-bond order ($b_{23} = 0.129$), further enhancing the 3-center character of the F_3^- binding. As shown in the natural atomic valency (V_A) values of Table 1, the F valencies all remain safely within the expected monovalency of the halogen family, thus confirming that no "expansion of the valence shell" or "d-orbital participation" is required[24] for 3c/4e hypervalency in this species, consistent with the negligible d-orbital occupancies that are found in natural population analysis (NPA) values.

Primary Long-Bonding in Neon Difluoride. An illustration of the surprising long-bond variant of 3c/4e hyperbonding is provided by the (experimentally unknown) neon difluoride (NeF_2) molecule, isoelectronic and isostructural to F_3^-. Although the "inert gas" Ne normally resists chemical associations of any type[25] (showing, e.g., no significant attraction to a single F atom), it is predicted to unite with *two* fluorine atoms to form a fairly robust linear triatomic species with equilibrium bond length ($R_{NeF} = 1.874$ Å) that is only ~0.1 Å beyond that of its F_3^- analogue. The NeF_2 species is only locally stable (metastable), lying about 69 kcal/mol above the Ne + 2F atomic dissociation limit and protected by an activation barrier of only about 9 kcal/mol from the about 80° bending deformation that "breaks" the hyperbond and expels Ne from the F_2 moiety, as shown in Figure 1. However, the linear equilibrium species exhibits robustly positive frequencies, thus establishing its stability with respect to small geometry distortions.

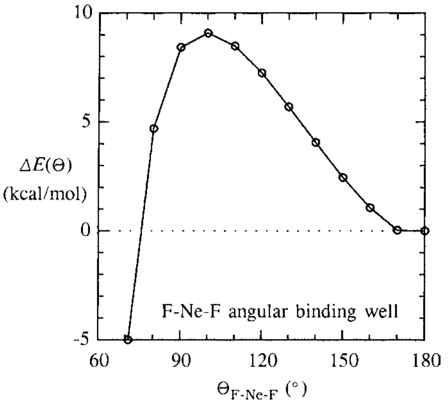

Figure 1. Calculated angular deformation potential $\Delta E(\Theta)$ for metastable NeF_2, showing the ~80° bend (and ~9 kcal/mol activation energy) needed to "break" the 3c/4e $\hat{\sigma}$-bond.

The isoelectronic and isostructural similarities of NeF_2 and F_3^- may suggest that these species employ similar 3c/4e bonding motifs. However, both the default $\hat{\sigma}$-bonded NBO structure of NeF_2 and its predominant w_{III} (73.7%) vs $w_{I,II}$ (13.1%) NRT weightings (leading to bond orders $b_{FF} = 0.74$, $b_{NeF} = 0.13$) establish that $\hat{\sigma}$-type *long*-bonding is the principal 3c/4e "chemical magic" of this species. The extraordinary $\hat{\sigma}_{FF}$ long-bond qualifies as a "shared electron pair" (NBO occupancy: 1.9993e) in the classical Lewis sense, but the equilibrium F−F bond length

$$R_{FF} = 3.75\text{Å} \tag{15}$$

far exceeds that of any known single-bond length between first-row atoms. Consistent with 12b, the F−Ne−F triad exhibits the inverted pattern for natural electronegativity values ($\Xi_{Ne} = 4.44$, $\Xi_F = 3.89$)

$$\Xi_{Ne} > \Xi_F \tag{16}$$

that promotes long-bonding. The highly unusual NeF_2 species may be considered prototypical of $\hat{\sigma}$-type 3c/4e long-bonding in late periods of the main group, thus demonstrating the feasibility of this bonding motif also in species of high Ξ_{av} that are far from the expected range of metallic behavior.

Figure 2 compares overlap contour diagrams for the leading NBO interactions associated with 3c/4e ω-bonding (Figure 1a) or $\hat{\sigma}$-bonding (Figure 1b) in F_3^- or NeF_2, respectively. Each panel also includes the associated second-order perturbative estimates ($\Delta E^{(2)}{}_{D\to A}$) of NBO donor−acceptor stabilization, consistent with powerful NRT resonance mixings found for both F_3^- and NeF_2.

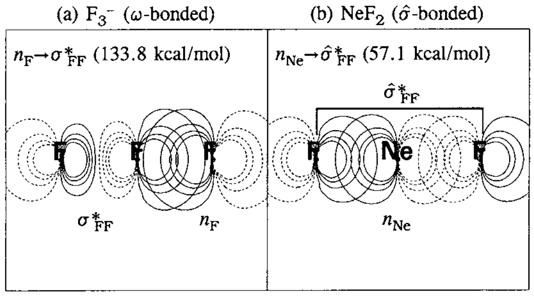

Figure 2. NBO orbital contour diagrams for leading $n_A \to \sigma^*_{LL'}$ delocalizations in (a) ω-bonded F−F−F$^-$, (b) $\hat{\sigma}$-bonded F−Ne−F.

As shown in the right panel of Figure 2, the n_{Ne} donor NBO is of p-type, leading to strong overlap with the *out*-of-phase $\hat{\sigma}^*_{FF}$ acceptor orbital. Consistent with (13b), NeF_2 therefore displays the expected characteristics of $\hat{\sigma}$-bonding, including the powerful central atom lone pair to "long antibond" ($n_A \to \hat{\sigma}^*_{LL'}$) delocalization that stabilizes this distinctive 3c/4e motif.

We may also compare the NeF_2 and F_3^- species in terms of alternative MO- or Quantum Theory of Atoms in Molecules (QTAIM)-based bonding criteria. Figure 3 illustrates the visual comparison of MO phase patterns for three critical MOs that might be expected to most directly display the critical $\hat{\sigma}/\hat{\sigma}^*$-type vs ω-type resonance features: lowest unoccupied MO (LUMO) (MO 15; most directly reflecting $\hat{\sigma}^*$ vs σ^* acceptor character); highest occupied MO (HOMO) (MO 14; most directly reflecting $\hat{\sigma}$ vs σ bond character); MO 7 (most directly reflecting central n_{Ne} vs $n_{F(-)}$ donor character). (Additional details of NBO vs MO comparative descriptions for HeF_2, NeF_2, and ArF_2 are presented in Supporting Information **S1**.) Although quantitative differences are evident in Figure 3, the unphysical mixings of MOs (based on angular rather than dynamical symmetries)[26] effectively disguise the distinct NBO/NRT bonding characteristics of these species. Recognition of long-bonding is also problematic for QTAIM-type bonding descriptors,[27] based on presence or absence of a topological bond critical point (BCP) in the electron density function. No such BCP is found for the $\hat{\sigma}_{FF}$ long-bond of NeF_2, because the large spillover density from the central Ne atom swamps the region of the associated natural bond critical point (NBCP)[28]

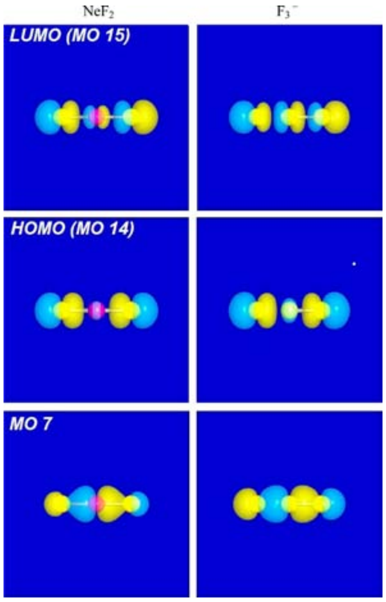

Figure 3. Comparison MOs of NeF$_2$ and F$_3^-$ (see text). (Surface contour values and other parameters of the optical model are identical to those for NBO visualizations.).

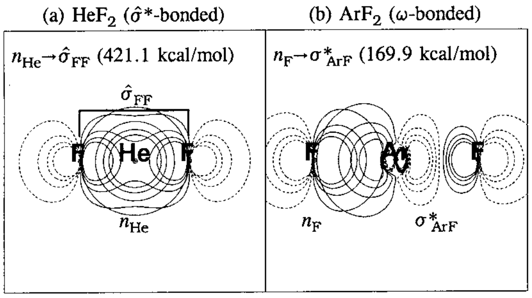

Figure 4. Similar to Figure 2, for (a) $\hat{\sigma}$*-bonded F−He−F, (b) ω-bonded F−Ar−F.

and converts the expected topological (3,1) saddle point to a cusp-type *maximum* in the total electron density function.

Other Main- and Transition-Group Long-Bonds. Table 1 includes energetic, geometric, and NBO/NRT descriptors for a variety of L-A-L′ hyperbonded triatomics, including final classification of 3c/4e type for F$_3^-$, NeF$_2$ (first two rows), and other species to be discussed below. The table includes the binding energy (with respect to atoms or ions), bond length, atom charges, and NRT weightings of the three principal 3c/4e resonance structures, as well as the associated $\Delta E^{(2)}{}_{D\to A}$ donor−acceptor stabilization for the principal hyperbonded form ($\omega/\hat{\sigma}/\hat{\sigma}^*$). (In each case, structures **I**, **II**, **III** are found to compose 100% of the NRT expansion, so NRT bond orders and resonance weightings are equivalent if the latter are expressed in fractional rather than percentage value, namely, $b_{AL} = w_I = w_{II}$, $b_{LL'} = w_{III}$.)

To explore further aspects of 3c/4e long-bonding and its dependence on central-atom electronegativity and angular donor type, we first examine the analogous rare-gas difluorides (F-Rg-F) for He and Ar (with Ξ_{He} = 4.04, Ξ_{Ar} = 3.12). As shown in the third and fourth rows of Table 1, both HeF$_2$ and ArF$_2$ form metastable linear triatomics that are apparently analogous to NeF$_2$. Unlike the latter, however, ArF$_2$ (with $\Xi_{Ar} - \Xi_F < 0$; n_{Ar} = p-type) favors ω-bonding, whereas HeF$_2$ (with $\Xi_{He} - \Xi_F > 0$; n_{He} = s-type) favors $\hat{\sigma}^*$-bonding. The leading $\Delta E^{(2)}{}_{D\to A}$ values for HeF$_2$ (n_{He}-σ_{FF}: 421 kcal/mol) or ArF$_2$ (n_F-σ^*_{ArF}: 170 kcal/mol) are even more strongly stabilizing than those for F$_3^-$ or NeF$_2$, yet only marginally sufficient to overcome the strong steric repulsions that oppose the tightly packed geometry of these filled-shell species. NBO contour plots of the leading HeF$_2$, ArF$_2$ delocalizations are shown in Figure 4 for comparison with corresponding NeF$_2$ delocalizations of Figure 2b.

Note the beautifully matched donor−acceptor lobe patterns that stabilize the triad in each figure panel: the s-type n_{He} donor NBO of the central helium atom that overlaps the p_F-type inner lobes of the $\hat{\sigma}_{FF}$ acceptor NBO in (a), and the p-type n_F donor NBO that overlaps the prominent p_{Ar}-type backside lobe of the σ^*_{ArF} acceptor NBO in (b). The properties of rare-gas difluorides displayed in Figures 2, 4 and Table 1 testify to the generality and strength of 3c/4e donor−acceptor delocalizations, leading to distinctive $\hat{\sigma}^*$-type (HeF$_2$), $\hat{\sigma}$-type (NeF$_2$), or ω-type (ArF$_2$) bonding motifs for entrapped Rg species of varying electronegativity and valence-shell angular symmetry. Of course, all these species are stabilized by resonance contributions from all three hyperbond structures, but those depicted in Figures 2, 4 carry primary weighting. Figure 5 compares the leading NBO bond motif for all three RgF$_2$ species in 3-d surface views, showing the contrasting phase patterns in long-bonding $\hat{\sigma}^*$ (HeF$_2$) or $\hat{\sigma}$ (NeF$_2$) vs conventional ω (ArF$_2$) 3c/4e motifs.

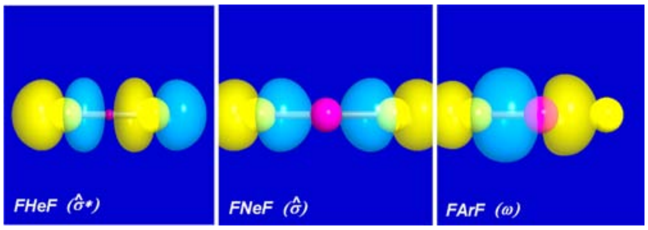

Figure 5. 3-d surface views of leading 3c/4e Lewis-type NBOs for RgF$_2$ species (Rg = He, Ne, Ar), showing contrasting phase patterns for $\hat{\sigma}^*$-type (He), $\hat{\sigma}$-type (Ne), and ω-type (Ar) bonding motifs (cf. Figures 2, 5).

Still more robust $\hat{\sigma}$-bonded triatomics are formed by monovalent *metal* atoms at the opposite end of the periodic row, such as the lithide analogues (Li-A-Li, A = Li, Be) of the first-row. Rows 5, 6 of Table 1 exhibit properties of hyperbonded Li$_3^-$ (electropositive ω-bond analogue of F$_3^-$) and isoelectronic BeLi$_2$ (electropositive $\hat{\sigma}^*$-bond analogue of HeF$_2$). Whereas the RgF$_2$ species are only metastably bound, the metallic Li$_3^-$ or BeLi$_2$ counterparts are calculated to be *absolutely* stable with respect to atomic or diatomic dissociation products, demonstrating the enhanced effectiveness of 3c/4e $\hat{\sigma}^*$-bonding for metal atoms. Because both He and Be are s-type valence donors, they exhibit the expected $\hat{\sigma}^*$-type hyperbonding motif, in contrast to the $\hat{\sigma}$-bonding motif of p-type Ne or Ar donors. Figure 6 displays contour plots and $\Delta E^{(2)}{}_{D\to A}$ values for the leading NBO delocalizations of the lithide species, allowing direct comparison with analogous fluoride delocalizations of Figures 2, 4.

Note that the hyperbonding interactions of Figure 6a,b primarily involve s-type NAOs on each center, as expected for s-block elements of the periodic table, but with significantly weaker $\Delta E^{(2)}{}_{D\to A}$ values than corresponding halide species of Figures 2, 4. This is partially due to reduced steric repulsions in

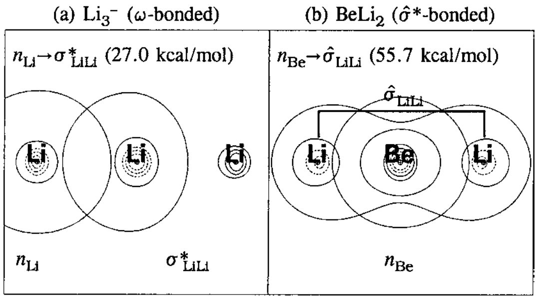

Figure 6. Similar to Figure 2, for (a) ω-bonded Li–Li–Li^-, (b) $\hat{\sigma}$*-bonded Li–Be–Li. Note that the σ^*_{LiLi} antibond of Figure 6(a) is so polarized that the Li atom at the right lacks the usual dashed contour line (at default contour setttings) delineating the effective van der Waals boundary of the valence region.

the early (metallic) species of the periodic row, which require weaker $\Delta E^{(2)}{}_{D\to A}$ attractions to achieve comparable net binding energy. However, the more important difference arises from *Rydberg*-type back-donation interactions involving low-lying 2p orbitals, particularly the strong $\hat{\sigma}^*{}_{LiLi}\to r^*{}_{Be}$ interaction (53.1 kcal/mol) that is shown for comparison with $n_{Be}\to\hat{\sigma}_{LiLi}$ in Figure 7.

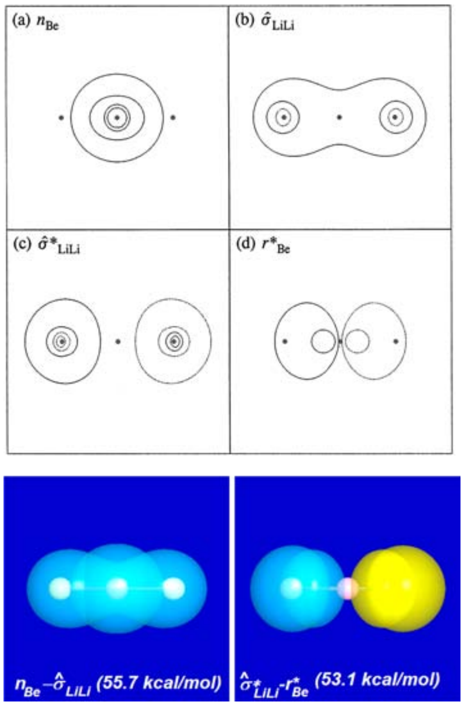

Figure 7. Reciprocally coupled NBO donor–acceptor pairs of $\hat{\sigma}$*-bonded LiBeLi, showing contour and surface views of n_{Be} lone-pair donor (a) and $\hat{\sigma}_{LiLi}$ long-bond acceptor (b) for principal $n_{Be}\to\hat{\sigma}_{LiLi}$ interaction (lower left; cf. Figure 6b), and long-bond $\hat{\sigma}^*{}_{LiLi}$ donor (c) and Rydberg-type $r^*{}_{Be}$ acceptor (d) for reciprocal $\hat{\sigma}^*{}_{LiLi}\to r^*{}_{Be}$ interaction (lower right).

Reciprocally paired donor–acceptor interactions such as shown in Figure 7 exhibit inherent *cooperativity* (mutual reinforcement and enhancement) and reduction of net charge transfer (capacitive build-up) that increasingly favors $\hat{\sigma}$-type long-bonding as s/p separation diminishes. This points strongly to increased propensity for $\hat{\sigma}$-long-bonding with increased nuclear charge Z and reduced electronegativity Ξ, consistent with the well-known diagonal banding pattern of metallic character in the periodic table. The complementary balance of charge transfer associated with reciprocal donor–acceptor interactions is also reflected in the net NPA atomic charges (Q_{Be} = −0.0063, Q_{Li} = +0.0032), which reflect essential *neutrality* across the triad.

We can also consider Group 11 (late monovalent halogen-like) elements of the transition-metal (TM) block, such as cupride analogues (Cu-A-Cu, A = Cu, Zn) of the first long transition series. The last two rows of Table 1 display hyperbonding properties of 14-electron, isoelectronic Cu_3^- (ω-bonded) and $ZnCu_2$ ($\hat{\sigma}$*-bonded) triads, showing the expected similarities to isovalent main-group halides. The metallic TM-hyperbond triads are again calculated to be absolutely stable with respect to atomic or ionic dissociation, with strong $\Delta E^{(2)}{}_{D\to A}$ stabilizations of expected form. As indicated in Table 1, $ZnCu_2$ is a somewhat borderline species, with only slightly greater NRT weighting for $\hat{\sigma}$-bond structure **III**, and with default NBO structure corresponding to **I** or **II**. Figure 8 shows orbital contour plots for the n_{Cu}-$\sigma^*{}_{CuCu}$ interaction of Cu_3^- (left) and n_{Zn}-$\hat{\sigma}_{CuCu}$ interaction of $ZnCu_2$ (right), for direct comparison with the main-group analogues of Figures 2, 4–6.

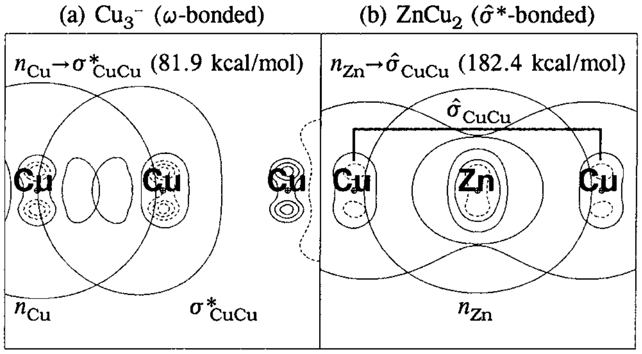

Figure 8. Similar to Figure 2, for (a) ω-bonded Cu–Cu–Cu^-, (b) $\hat{\sigma}$*-bonded Cu–Zn–Cu. Note again the extreme polarization of the σ^*_{LiLi} antibond of Figure 8(a), similar to Figure 6(a), which displays only a faint "backside" trace of the dashed contour for above-vdW values of valence density.

From Figure 8 one can recognize that $\hat{\sigma}$*-bonding is enhanced by the dominant s-type character of the central n_A donor, which promotes the strange-looking "long-antibond" NBO motif. As shown in the $\hat{\sigma}_{LL'}$ NBOs of Figures 6b, 8b, the diffuse NHOs of sufficiently electropositive terminal L atoms may give appreciable *direct* in-phase overlap, further enhancing the effectiveness of $\hat{\sigma}_{LL}$ as an acceptor for the central n_A donor. The $\hat{\sigma}$*-bonding motif therefore leads to the strongest $\Delta E^{(2)}{}_{D\to A}$ stabilizations of Table 1, and gains increasing advantage as Ξ_L decreases.

How is $\hat{\sigma}$*-bonding propensity affected by more general sp^λ (main-group) or sd^μ (transition-group) hybrid character of n_A? The qualitative answer can be deduced from the *parity* (inversion symmetry) of s-type (*gerade*), p-type (*ungerade*), and d-type (*gerade*) components of the bonding hybrids. The intrinsic *gerade* symmetry of n_A-$\hat{\sigma}_{LL}$ delocalizations is evidently preserved for arbitrary sd^μ hybrids of transition metals, but not for sp^λ hybrids of main-group elements. In a similar manner, it has been recognized (ref 1, p 447ff) that ω-bonding is far more prevalent in transition-group than main-group species, because the *gerade* symmetry of sd^μ TM hybrids insures *equal* hybrid amplitude (and bonding strength) in forward and backward directions, as required for the overall *gerade* symmetry of strong ω-bonding delocalization. TM species therefore gain important advantages over main-group species (except those of s-block Groups 1, 2) for 3c/4e delocalization of both ω and $\hat{\sigma}^*$ type, particularly for the latter in low-Ξ_L species. Thus, one can anticipate that the $\hat{\sigma}^*$ motif contributes significantly to the bonding in recently reported "molecular alloys" such as $Mo(M'R)_{12}$ and $M(M'R)_8$ (M: Pd, Pt, Mo; M′: Zn, Cd; R: Me=CH_3, Cp* = pentamethylcyclopentadienyl).[29]

As discussed previously [cf. (12a)], the propensity for L-A-L $\hat{\sigma}^*$-bonding is also expected to depend on the electronegativity *difference* ($\Delta\Xi = \Xi_A - \Xi_L$) between central and terminal atoms of the triad. Figure 9 exhibits this dependence for the neutral species of Table 1, showing the reasonable linear correlation between the NRT weighting of $\hat{\sigma}$ or $\hat{\sigma}^*$ resonance structure **III** and $\Delta\Xi$.

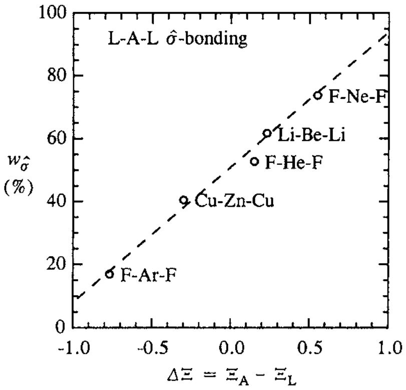

Figure 9. Dependence of $\hat{\sigma}$-bond resonance weighting w_{III} on natural electronegativity difference $\Delta\Xi$ (= $\Xi_A - \Xi_L$) for neutral hyperbonded L-A-L triads (cf. Table 1).

Overall, we can recognize that $\hat{\sigma}$-type long-bonding or $\hat{\sigma}^*$-type long-antibonding provides a surprisingly effective alternative binding mechanism for atomic triads of suitable valence angular symmetry and electronegativity. Particularly for the metallic s-block elements of the main group and many d-block TM species, $\hat{\sigma}^*$-bonding proves to be the preferred choice for achieving stable L-A-L triads. The ω-type vs $\hat{\sigma}^*$-type of hyperbonding therefore presents a choice of 3c/4e NBO bonding motifs, leading to profoundly different structural, vibrational, and spectroscopic signatures (as discussed below). Resonance hybridization allows a particular species to mix and match ω- vs $\hat{\sigma}^*$-bonding character to achieve best overall stability.

However, we can recognize the general dichotomy between (i) the typical *molecular* bonding pattern of strongly localized 2c/2e Lewis-like bonding skeleton, perturbatively stabilized by secondary 3c/4e ω-type resonance, vs (ii) the alternative $\hat{\sigma}^*$-type bonding pattern of weakly hybridized NHOs, with little or no directional focus, strongly stabilized by n_A-$\hat{\sigma}_{LL'}$ interactions. Although the delocalized $\hat{\sigma}^*$-type NBO motif **III** appears quite surprising compared to more conventional Lewis-structural forms such as **I**, **II**, it seems to open a unique 3c/4e pathway to delocalized binding in triads having no underlying 2c covalent bonds of conventional type. Thus, the conventional perturbative precedence ("correcting" the zeroth-order NLS for "weak" resonance-type donor−acceptor interactions) is *reversed* in the long-bonding regime, suggesting the *transitional* character (and likely activation barriers) associated with passage between ordinary and long-bonding domains.

II. THERMODYNAMICS AND KINETICS OF LONG-BOND FORMATION FOR $BeLi_2$ METALLIC TRIADS

As a representative example of $\hat{\sigma}$-triad formation from atomic and diatomic precursors, let us now consider the elementary main-group species Li−Be−Li (**1**; row 6 of Table 1), with characteristic $\hat{\sigma}^*$ (long-antibond) triad motif. Both Be and Li are of metallurgical as well as scientific interest,[30] and high-pressure Be/Li alloys have been predicted to exhibit superconductive properties.[31]

The first five rows of Table 2 summarize calculated thermodynamic ΔE (energy), $\Delta G°$ (standard-state Gibbs free energy) and other properties for equilibrium species of the $BeLi_2$ potential energy surface, expressed in per-atom form for convenient comparison with higher-order Be_nLi_m clusters to be considered below. Figure 10 displays ball-and-stick diagrams with leading NBOs and parenthesized energies (relative to free atoms) for the three equilibrium species (**1**, **2**, **3**) and connecting transition-state species (**1**−**2**‡, **2**−**3**‡) of the $BeLi_2$ potential energy surface.

Table 2. Calculated Per-Atom Energy and Standard-State Free Energy ΔE/atom, $\Delta G°$/atom[a], Electron Correlation Energy E_{corr}[b], and Static Polarizability[c] for Equilibrium σ-Bonded Precursors and $\hat{\sigma}$-Bonded $Li(BeLi)_n$ Linear Chains (n = 1−9), $BeLi_4$ (2-d), and $BeLi_6$ (3-d) metallic clusters, and cyclic $(BeLi)_{10}$ Species[d]

species	ΔE/atom	$\Delta G°$/atom	E_{corr}/atom	α_0/atom	α_{zz}
Be			−16.75	43.1	43.1
Li			0.00	143.4	143.4
BeLi	−5.37	−3.14	−8.48	87.6	303.0
Li_2	−10.40	−7.62	−5.91	99.0	261.7
$BeLi_2$ (**1**)	−12.22	−7.94	−11.58	92.4	528.3
Li···BeLi (**2**)	−8.60	−5.44	−11.18	80.4	161.0
Be···Li_2 (**3**)	−8.58	−5.36	−7.44	104.0	593.1
$Li(BeLi)_2$	−12.72	−7.75	−11.03	158.0	1940.0
$Li(BeLi)_3$	−12.88	−7.66	−13.62	162.7	2872.9
$Li(BeLi)_5$	−13.21	−7.82	−14.33	255.9	7667.7
$Li(BeLi)_7$	−13.39	−7.41	−14.70	369.7	15626.8
$Li(BeLi)_9$	−13.49	−5.17	−14.91	503.9	27482.1
$BeLi_4$	−18.14	−12.60	−12.78	80.6	205.0
$BeLi_6$	−23.60	−17.05	−14.91	65.9	461.6
c-$(BeLi)_{10}$	−13.79	−7.69	−10.29	50.3	516.8

[a]Formation from atoms; kcal/mol. [b]UMP2 frozen-core approximation; kcal/mol. [c]Per-atom isotropic average α_0/atom and molecular long-axis component α_{zz}; a.u. [d]Taken as closed-shell singlets, except for odd-electron Li, BeLi, Be_2Li_3.

Equilibrium and kinetic properties of $BeLi_2$ species under standard-state conditions are depicted by the calculated ΔE energy level diagram in Figure 11a. (The corresponding standard-state $\Delta G°$ levels of Figure 11b are qualitatively similar.) As shown in the diagram, the $\hat{\sigma}^*$-bonded species **1** is the global minimum, lying about 11 kcal/mol below σ-bonded "Be···Li_2" isomers **2** (L-shaped) and **3** (linear) and separated from these species by an about 10 kcal/mol transition

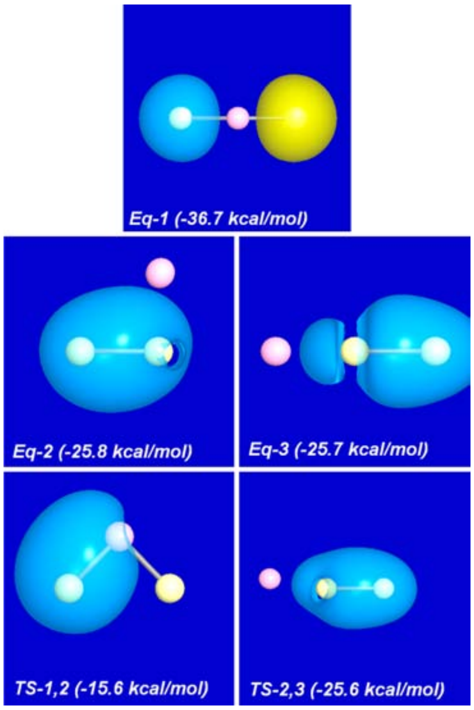

Figure 10. NBOView diagrams (and parenthesized energies, relative to free atoms) for molecular structure and principal bonding NBO of equilibrium structures **1**–**3** (upper panels) and transition species (lower panels) of the $BeLi_2$ potential energy surface (cf. Table 2, Figure 11).

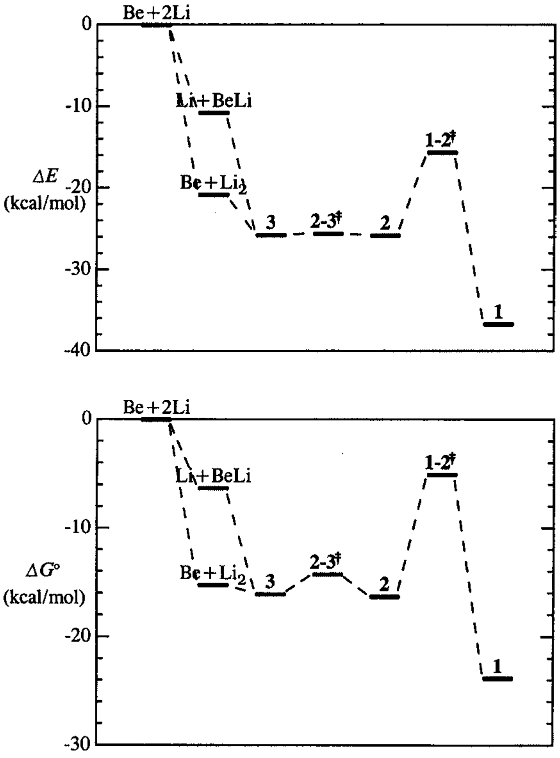

Figure 11. Calculated ΔE energy levels (a; upper) and standard-state $\Delta G°$ free energy levels (b; lower) for equilibrium and transition state species of the triatomic $BeLi_2$ potential surface (cf. Table 2), expressed with respect to dissociated Be + 2Li atoms.

state activation barrier (similar in magnitude to that of Figure 1). As shown in Figure 10, the **1**–**2**‡ transition species is C_{2v}-symmetric (ca. 90° Li–Be–Li bond angle), best described as the ω-type 3c/4e resonance hybrid of $Li{-}Be^{+}\cdots Li^{-}$ and $Li^{-}\cdots Be{-}Li^{+}$ resonance forms. The **1**–**2**‡ transition species may therefore be considered as the high-energy "portal" that separates the molecular (σ-type) and metallic ($\hat{\sigma}^{*}$-type) bonding domains.

According to the energy levels shown in Figure 11, gas-phase atoms or diatomic species are expected to follow essentially barrierless pathways to form metastable complexes **2** or **3**, kinetically trapped by the relatively high **1**–**2**‡ transition barrier. Formation of the metallic isomer **1** is therefore problematic under molecular beam conditions, challenging experimental characterization of long-bonded triads. Despite such difficulties, the apparent role of $\hat{\sigma}^{*}$-bonded $BeLi_2$ as the fundamental nucleating agent and "building block" for Be/Li metallic phase formation amply justifies theoretical characterization of its monomeric and higher-order aggregation properties, as sketched below.

The DFT energy levels, geometries, and NBO forms of Figures 10, 11 appear to agree reasonably with those found at MP2 or other theoretical levels. At the fixed DFT geometry of Figure 10, the MP2/6-311++G** atomization energy ΔE_{atom} of **1** is significantly reduced (to 27.6 kcal/mol, vs DFT 36.7 kcal/mol), but the calculated exothermicity with respect to **2** ($\Delta E_{2\to1}$ = −10.5 kcal/mol, vs DFT −10.9 kcal/mol) is virtually unchanged. The MP2-optimized R_{LiLi} distance of **1** increases slightly (from 5.01 to 5.05 Å), but the MP2 NBOs consistently exhibit the same $\hat{\sigma}^{*}$-type motif seen in DFT calculations. Thus, the adopted B3LYP/6-311++G** methodology appears adequately representative for present exploratory purposes.

At the B3LYP/6-311++G** level, all species of Figure 10 are found to be closed-shell singlets, electronically stable with respect to diradical UHF or higher-multiplicity character. However, the extreme Li···Li separation and indirect (Be-mediated) e-pairing interactions of **1** suggest that relatively low-lying diradical singlet and triplet states may be a characteristic feature of the excitation spectrum. The vertical singlet–triplet splittings can be obtained either from direct DFT differences (viz., $\Delta E_{\mathrm{ST}} = {}^{3}E_{\mathrm{B3LYP}} - {}^{1}E_{\mathrm{B3LYP}}$) or corresponding TD-DFT estimates. For **1**, the direct ΔDFT (or TD) estimate of ΔE_{ST} is found to be 19.7 kcal/mol (or 15.0 kcal/mol), significantly smaller than corresponding estimates for precursor species Be [56.7 (or 48.2) kcal/mol] or Li_2 [25.1 (or 23.2) kcal/mol]. Further evidence of low-lying triplet character in $\hat{\sigma}^{*}$-bonded species will be presented in examples to follow.

III. LONG-BONDING IN HIGHER BE$_N$LI$_M$ METAL CLUSTERS

How does $\hat{\sigma}$-type long-bonding lend itself to higher-order clustering and condensation phenomena? To briefly address this question for a representative case, we now consider generalizations of the simple $BeLi_2$ $\hat{\sigma}^{*}$-bonded triad to extended 1-dimensional chains as well as analogous 2 and 3-dimensional bonding motifs.

One-Dimensional Long-Bonding. Let us first consider the cohesive, mechanical, and electrical properties of extended linear chains, as summarized for selected Be_nLi_{n+1} species (up to n = 9) in rows 8–12 of Table 2, focusing primary attention on odd-n species of singlet spin multiplicity. As seen in the table entries, the per-atom cohesive energy (ΔE/atom) apparently continues to increase beyond the chain lengths considered in

Table 2, leading to eventual saturation only in the high-n limit. However, the corresponding standard-state $\Delta G°$/atom free energy values exhibit a maximum near $n = 5$, suggesting that equilibration will lead to a mixture of smaller chain-length species under standard-state conditions. Thermal and pressure effects will evidently play a significant role in controlling equilibrium chain-length distributions.

[It should be mentioned that low-lying triplet or multiradical states are increasing sources of electronic instability in higher Be_nLi_m clusters, as might be anticipated from Hund's rule. Indeed, formal triplet DFT states (of severe spin contamination) are generally found to lie *lower* than the singlet states for all $Li(BeLi)_n$ linear chains with $n > 1$, as well as other species considered below. However, in the present work we have chosen to focus on the singlet surface, ignoring spin-forbidden triplet or higher multiplicity components that may contribute to the ground-state density matrix of the physical system at finite temperatures.]

Higher $\hat{\sigma}^*$-bonded Be_nLi_{n+1} chains also show unusual vibrational properties compared to molecular σ-bonded species. Figure 12 displays calculated harmonic vibrational frequencies for odd-n (singlet) species up to $n = 9$. As shown in Figure 12, a dense band of vibrational levels is seen to form at very low frequencies (0−40 cm^{-1}), and another such band forms around 100 cm^{-1}, far below the usual range of molecular torsional, bending, and stretching modes.

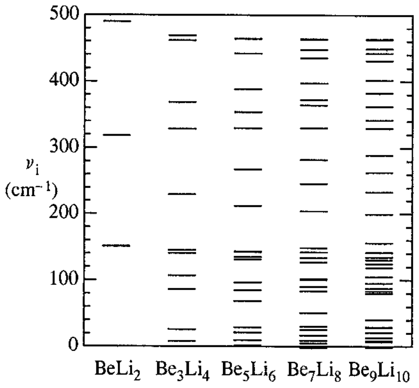

Figure 12. Calculated harmonic vibrational frequencies (cm^{-1}) of $\hat{\sigma}^*$-bonded $Li(BeLi)_n$ chains.

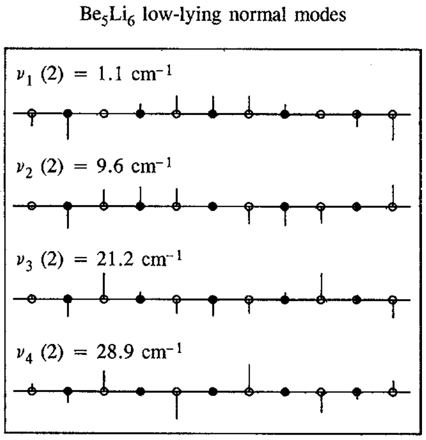

Figure 13. Normal modes of Be_5Li_6, showing "standing-wave" displacement vectors of low-frequency degenerate vibrations along the metal chain.

The character of the extreme low-frequency modes of $\hat{\sigma}^*$-bonded chains can be seen in Figure 13, which displays normal-mode displacement vectors for the four lowest vibrational modes of Be_5Li_6 (each doubly degenerate). As seen in Figure 13, these displacement vectors exhibit the characteristic standing-wave patterns of a vibrating string, with an additional half-wave for each increment of vibrational quantum number. Such collective motions reflect the "rope-like" suppleness of the overall metallic chain, quite distinct from the usual bond-type stretch, bend, and twist modes that characterize molecular species. The lowest band of transverse (x, y) modes in the 0−40 cm^{-1} range is followed by a similar band of "spring-like" longitudinal compression (z) modes centered around 100 cm^{-1}, all corresponding to ultrasoft *collective* motions with no counterpart in typical molecular species. Thus, the mechanical, rheological, and calorimetric properties of metallic $\hat{\sigma}^*$-bonded chains can be expected to differ *qualitatively* from those of common organic polymers. Note that short-wavelength transverse modes tend to bend $\hat{\sigma}^*$-bonded triads out of favorable linearity, hence affecting the donor−acceptor interactions and associated electronic properties of the idealized equilibrium linear chains. This points to potentially important thermal effects on vibrational-electronic couplings that may control the onset of $\hat{\sigma}^*$-bonding phenomena.

As shown in the final two columns of Table 2, extraordinary electronic behavior is also evident in calculated polarizability components $\{\alpha_{ij}\}$, particularly the α_{zz} component along the chain axis. Each polarizability component describes the vectorial charge displacement (change in dipole moment $\boldsymbol{\mu}$) in response to an external electric field $\mathbf{F}$, namely,

$$\alpha_{ij} = \partial \mu_i / \partial F_j \quad (i, j = x, y, z) \tag{17}$$

The limiting case $\alpha_{zz} \to \infty$ therefore corresponds to an idealized *electrical conductor*, unable to resist field-induced charge flow along the field direction. As shown in the final column of Table 2, the $\hat{\sigma}^*$-bonded Be_nLi_{n+1} chains exhibit remarkably rapid convergence toward this "ideal conductor" limit. The calculated longitudinal polarizability of $BeLi_2$ (528 au) is already surprisingly large compared to precursor Be or Li_2 values (43 and 262 au, respectively). However, each chain extension leads to further explosive growth, roughly *doubling* α_{zz} with each $n \to n+2$ increment along the singlet sequence. The exponential growth pattern is evident even when plotted in muted form as the isotropic average polarizability value [$\alpha_0 = (\alpha_{xx} + \alpha_{yy} + \alpha_{zz})/3$] on a per-atom basis (column 4), as shown in Figure 14. Such extraordinary electrical permittivity is quite unlike that of conventional σ-bonded polymeric species, signaling an entirely new domain of $\hat{\sigma}^*$-based electronic phenomena. It should not escape attention that the transition from σ-type to $\hat{\sigma}^*$-type bonding motifs suggests aspects of a *structural phase transition* that may relate to onset of characteristic conductive or superconductive phase behavior.

The electronic properties of linear $Li(BeLi)_n$ chains also appear exceptional with respect to the magnitude of electron correlation (E_{corr}) effects. As shown in column 3 of Table 2 and plotted in Figure 15, the magnitude of valence-shell dynamic correlation energy (as estimated at frozen-core MP2 level) increases impressively with increased $\hat{\sigma}^*$-bonded chain length. According to the general theory of dynamic electron correlation effects in atomic and molecular species,[32] such increase might reasonably be attributed to progressive increases in bond-type "left-right" correlations, which allow spin-paired electrons to

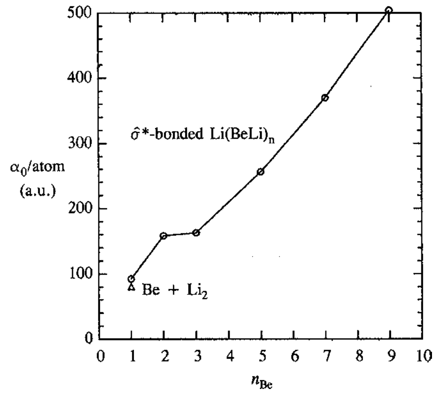

Figure 14. Isotropically averaged static dipole polarizability α_0 for linear $\hat{\sigma}$*-bonded Li(BeLi)$_n$ chains, expressed on a per-atom basis to show exponential growth along the chain direction [cf. Be + Li_2 precursor species (triangle)].

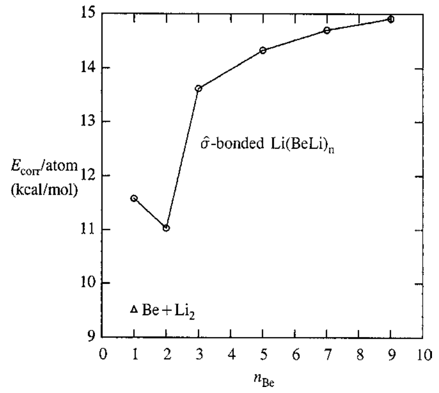

Figure 15. Electron correlation energy E_{corr} [MP2(FC)/6-311++G** estimate] for linear $\hat{\sigma}$*-bonded Li(BeLi)$_n$ chains, expressed on a per-atom basis to show gradual increase and saturation with increasing chain length [cf. Be + Li_2 precursor species (triangle)].

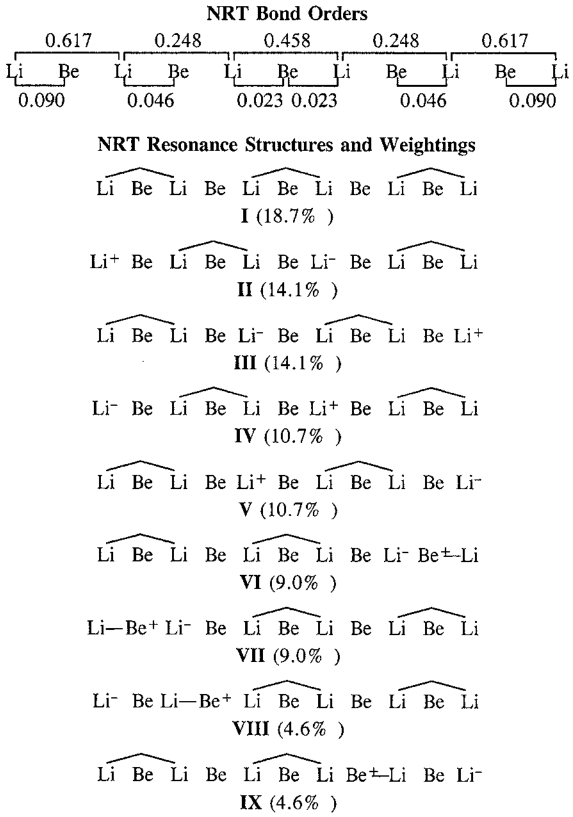

Figure 16. NRT bond orders (upper) and the associated principal resonance structures **I**–**IX** (with parenthesized weightings) for $\hat{\sigma}$*-bonded Be_5Li_6.

dynamically separate toward opposite ends of a chemical bond and thereby reduce Coulombic repulsions. In $\hat{\sigma}$-type long-bonding, such left-right correlations evidently gain effectiveness through the increased separation of coherently bonded centers. The evidence of Figure 15 is that some type of higher-order resonance-type coherence in longer Li(BeLi)$_n$ chains continues to extend the effective range of dynamical left-right correlation stabilization up to a long-range saturation limit.

The nature of long-range resonance-type effects in $\hat{\sigma}$*-bonded chains can be investigated more directly with NRT analysis of the DFT density. Figure 16 summarizes the composite NRT bond orders of long-bond ($\hat{\sigma}$) and short-bond (σ) type, together with weightings and other details of leading resonance structures **I**–**IX** (not to be confused with generic resonance labels of Sec. II). As seen in the NRT bond orders, long-bonding is the clearly dominant feature of the metal chain (b_{long} = 0.2–0.6 vs b_{short} < 0.1). The pure long-bonded resonance form **I** gains highest weighting (19%), followed by mixed ionic/long-bond ($Li^+\cdots Li^-$) forms **II**–**V** (11–14% each) and lesser ω-type (Li^- Be^+-Li) and σ-type **VIII**–**IX** contributions. The summed bond orders about each atom also allow one to see that the natural valency of each Li atom is significantly reduced from monovalency (V_{Li} = 0.71, 0.91, 0.73 from each chain-end) and that of Be is near-zero (V_{Be} = 0.09, 0.05, 0.05), quite different from "normal" values found in molecular species. All these results point to long-range delocalization and coupling effects that are quite extraordinary from a molecular viewpoint.

Two- and Three-Dimensional Long-Bonding. We may also briefly examine aspects of $\hat{\sigma}$-type long-bonding in higher dimensions. Rows 13, 14 of Table 2 exhibit the effect of encapsulating the central Be atom with additional Li^Li long-bonds in 2-d ($BeLi_4$) and 3-d ($BeLi_6$) species. As seen in the ΔE, $\Delta G°$ values, such dimensional extensions are *strongly* favored, suggesting synergistic enhancements of 1-d long-bonding features described above. Electron correlation is also enhanced, presumably by additional angular screening and separation modes that become available in higher dimensions. As expected, the electric polarizability becomes more isotropic, but also appears somewhat muted compared to 1-d $BeLi_2$, suggesting that effective dimensionality is an important control factor in optimizing anisotropic long-bond conduction properties.

Finally, we can also consider using the suppleness of transverse bending distortions to construct 2-d *cyclic* (BeLi)$_n$ chain species that may emulate aspects of the infinite 1-d Li(BeLi)$_n$ chain limit.[33]

The first member of this series, $(BeLi)_2$, adopts a stable $\hat{\sigma}$*-type Li^Li-bonded diamond-shaped (D_{2h}) geometry with *both* beryllium lone pairs participating in strong $n_{Be} \rightarrow \hat{\sigma}^*_{LiLi}$ donor–acceptor stabilizations. Figure 17 displays surface views of the $\hat{\sigma}^*_{LiLi}$ (a) and n_{Be} (b) Lewis-type NBOs, as well as the stabilizing $n_{Be} \rightarrow \hat{\sigma}_{LiLi}$ interaction (c). Although obviously not a true linear-chain analogue, this species illustrates how *multiple* Be donors may be able to surround and stabilize a single Li^Li long-bond (within limitations of steric crowding), leading to

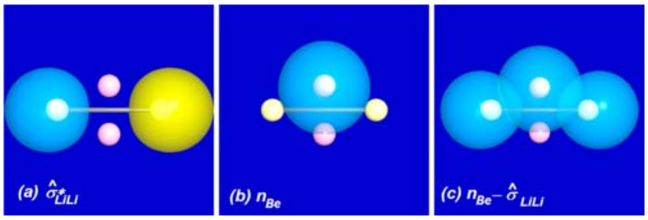

Figure 17. Be_2Li_2 Lewis-type NBOs $\hat{\sigma}^*_{LiLi}$ (a) and n_{Be} (b), with principal $n_{Be} \rightarrow \hat{\sigma}_{LiLi}$ donor−acceptor interaction (c).

Be-enriched stoichiometries. However, further details of such Be-girded chains are beyond the scope of present discussion.

The next members of the $(BeLi)_n$ even-*n* sequence, *n* = 4−8, optimize to near-cyclic *transition*-state species (with 2−9 imaginary frequencies), indicating instabilities with respect to noncyclic distortions that disrupt the quasi-linear conjugation chain. Such structures are not considered further.

However, the *n* = 10 member [$(BeLi)_{10}$, "cyclodeca-BeLi"] successfully optimizes to the cyclic structure shown in Figure 18. This species exhibits *five* $\hat{\sigma}^*_{LiLi}$ long-bonds in each of the two equivalent Kekulé-like resonance forms obtained by NRT. The final row of Table 2 compares this "c-$(BeLi)_{10}$" species with other Be_nLi_m species considered above. Although subject to considerable ring strain, c-$(BeLi)_{10}$ seems to anticipate certain aspects of the $n \rightarrow \infty$ infinite chain limit and suggests the atomic-level "malleability" that presents a quite novel palette of structural and electronic possibilities compared to covalently bonded molecular species.

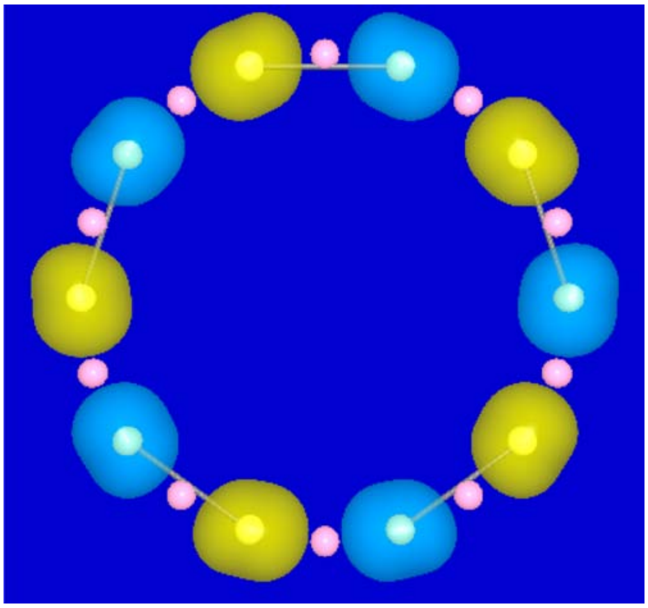

Figure 18. Lewis-type NBOs of cyclic $(BeLi)_{10}$, showing one of two equivalent Kekulé-like structures for the five $\hat{\sigma}^*_{Li-Li}$ long-bonds.

As in linear $Li(BeLi)_n$ species discussed previously, the ground states of cyclic $(BeLi)_n$ species are found to be of higher spin multiplicity. In the geometry of Figure 18, for example, an open-shell multiradical state of $\langle S^2 \rangle$ = 4.48 (or 14.40 after annhilation of the first spin contaminant) lies 51.76 kcal/mol below the closed-shell singlet. The NBO description of the open-shell cyclic multiradical is also remarkable.[32] Each long-bonded triad Li′BeLi″ of the singlet is replaced by two *anti*bonding spin-NBOs $\sigma^*_{BeL'}$ and $\sigma^*_{BeLi''}$ of polarized form, namely,

$$\sigma^*_{BeLi'} = 0.80(sp^{1.00})_{Be} - 0.60(sp^{0.10})_{Li'}$$

(occupancy 0.912e)

flanked by Be s-type nonbonding spin-NBOs (occupancy 0.921e) on either end. (In the opposite spin set, the "antibonding" vs "flanking" role of each Be atom is reversed.) Each antibonded triad is stabilized by geminal hyperconjugative delocalizations of $\sigma^*_{BeLi'} \rightarrow \sigma_{BeLi''}$ form (each with estimated 15.6 kcal/mol $E^{(2)}_{DA}$), which apparently provide the driving force for this counterintuitive NLS motif.

The distinguishing feature of both closed- and open-shell variants of metallic 3c/4e LiBeLi triads is thereby seen to be the *dominant role of donor−acceptor stabilizations*, despite the apparent *in*stability of an underlying Lewis-like pattern. In this respect, such metallic 3c/4e motifs differ *qualitatively* from the molecular motifs (with stable Lewis-like pattern) that underlie chemical bonding theory. We conclude that such strikingly different NBO motifs accurately signal the fundamental property shifts and activation barriers that differentiate "molecular" vs "metallic" behavior, and can therefore serve as a unifying conceptual framework to better understand these distinct domains of electronic behavior.[34]

IV. SUMMARY AND CONCLUSIONS

We have identified a counterintuitive NBO "bond" (2-center shared electron pair) motif that is aptly identified as a "long-bond," with record-setting interatomic separation that *far* exceeds conventional covalent bond length. The long-bonding 3c/4e motif appears as the characteristic transitional feature that bridges molecular (directed covalency) and metallic (near-free electron) limits of electronic binding. The $\hat{\sigma}$-type motif (denoted A^B, whether of in-phase $\hat{\sigma}_{AB}$ or out-of-phase $\hat{\sigma}^*_{AB}$ character) was shown to underlie the remarkable binding of HeF_2 and NeF_2, as well as other surprising main- and transition-group metallic triads. We described the characteristic NBO/NRT properties of A^B bonding and the relationship to electronegativity, valence-shell occupancy, donor−acceptor orbital parity, and other features of 3-center, 4-electron hypervalency, employing the prototype $BeLi_2$ triad to illustrate the distinctive structural, vibrational, and polarizability properties of extended linear chains, rings, and other long-bonded 1/2/3-d Be_nLi_m clusters. Still other examples of long-bonding are found in pure metallic clusters such as Li_9 that are representative of bulk crystallographic structure.[35]

All such examples are found to illustrate the *qualitative* distinction between covalent σ-bonding and $\hat{\sigma}/\hat{\sigma}^*$ long-bonding, pointing to the close association of the latter with recognized mechanical, electrical, and calorimetric signatures of metallicity. We conclude that the novel $\hat{\sigma}/\hat{\sigma}^*$-type long-bonding motif (or its easily envisaged pi-type analogue, etc.) represents an important addition to the list of currently recognized chemical bonding "types," offering improved chemical understanding of the interface between molecular and metallic domains of electronic binding.

■ ASSOCIATED CONTENT

Ⓢ Supporting Information

Two supporting documents are provided: (S1) "Relationship to Molecular Orbital Description" (supplementing discussion of Figure 3); (S2) "Energies and Coordinates of Optimized

Species" (supplementing triatomic data of Table 1). This material is available free of charge via the Internet at http://pubs.acs.org.

AUTHOR INFORMATION

Corresponding Author

*E-mail: landis@chem.wisc.edu.

Notes

The authors declare no competing financial interest.

ACKNOWLEDGMENTS

We thank UW-Chemistry Computational Chemistry Facility (NSF CHE-0840494) for partial computational support.

REFERENCES

(1) Weinhold, F.; Landis, C. R. *Valency and Bonding: A Natural Bond Orbital Donor-Acceptor Perspective*; Cambridge University Press: Cambridge U.K., 2005; p 281ff.

(2) Kittel, C. *Introduction to Solid State Physics*, 7th ed.;Wiley: New York, 1995, p 161ff.; Mott, N. F.; Jones, H. *The Theory of the Properties of Metals and Alloys*; Dover: New York, 1958.

(3) Weinhold, F. Natural Bond Orbital Methods. In *Encyclopedia of Computational Chemistry*; P. v.R. Schleyer, Allinger, N. L., Clark, T., Gasteiger, J., Kollman, P. A., Schaefer, H. F., III, Schreiner, P. R., Eds.; John Wiley: Chichester, U.K., 1998; Vol. 3, pp 1792−1811; Glendening, E. D.; Landis, C. R.; Weinhold, F. *WIREs Comput. Mol. Sci.* **2012**, *2*, 1−42 ; http://nbo6.chem.wisc.edu/.

(4) Weinhold, F.; Landis, C. R. *Discovering Chemistry With Natural Bond Orbitals*; Wiley: Upper Saddle River, NJ, 2011.

(5) For standard computational method and basis set acronyms used herein, see: Foresman, J. B.; Frisch, A.E. *Exploring Chemistry With Electronic Structure Methods: A Guide To Using Gaussian*, 2nd ed.; Gaussian, Inc.: Pittsburgh, PA, 1995.

(6) Glendening, E. D.; Weinhold, F. *J. Comput. Chem.* **1998**, *19*, 593−609. ; 610−627. Glendening, E. D.; Badenhoop, J. K.; Weinhold, F. *J. Comput. Chem.* **1998**, *19*, 628−646.

(7) Reed, A. E.; Curtiss, L. A.; Weinhold, F. *Chem. Rev.* **1988**, *88*, 899−926 ; Ref 1, p 16ff..

(8) Parr, R. G.; Yang, W. *Density-Functional Theory of Atoms and Molecules*; Oxford University Press: London, U.K., 1994.

(9) Jensen, W. B. *J. Chem. Educ.* **1995**, *72*, 395−398.

(10) A. E. Van Arkel *Molecules and Crystals*; Butterworths: London, U.K., 1949.

(11) Allen, L. C. *J. Am. Chem. Soc.* **1992**, *114*, 1510−1511.

(12) Landis, C. R.; Cleveland, T.; Firman, T. K. *J. Am. Chem. Soc.* **1995**, *117*, 1859−1860. Landis, C. R.; Firman, T. K.; Root, D. M.; Cleveland, T. *J. Am. Chem. Soc.* **1998**, *120*, 1842−1854 ; Ref 1, pp 365−420.

(13) Mednikov, E. G.; Dahl, L. F. *Phil. Trans. R. Soc. A* **2010**, *368*, 1301−1332.

(14) Sevov, S. C. Zintl Phases. In *Intermetallic Compounds; Principles and Practice*; Westbrook, J. H., Fleischer, R. L., Eds.; Wiley: Chichester, U.K., 2002; pp 113−132.

(15) As noted by Jensen: Jensen, W. B. *J. Chem. Educ.* **2009**, *86*, 278−279. "The metallic bond has had a very spotty history in the chemical literature." Among notable efforts to wrestle with this concept from a chemical viewpoint, see, e.g. Pauling, L. *Nature of the Chemical Bond*, 3rd. ed.; Cornell University Press: Ithaca, NY, 1989; Chapter 11 ; Hoffmann, R. *Solids and Surfaces: A Chemist's View of Bonding in Extended Structures*; VCH Publishers: New York, 1988; Burdett, J. K. *Chemical Bonding in Solids*; Oxford University Press: New York, 1995; Guo, Y.; Langlois, J.-M.; Goddard, W. A., III *Science* **1988**, *239*, 896−899. Anderson, W. P.; Burdett, J. K.; Czech, P. T. *J. Am. Chem. Soc.* **1994**, *116*, 8808−8809. Allen, L. C.; Capitani, J. F. *J. Am. Chem. Soc.* **1994**, *116*, 8810. Schön, J. C. *Angew. Chem., Int. Ed.* **1995**, *34*, 1081−1083 , and ensuing discussion.

(16) For a chemically oriented approach to solids, see: Harrison, W. A. *Electronic Structure and the Properties of Solids: The Physics of the Chemical Bond*; Dover: New York, 1989.

(17) The *Wikipedia* entry for "metallic bond" declares firmly: "...this type of bonding is collective in nature and a single 'metallic bond' does not exist" (http://en.wikipedia.org/wiki/Metallic_bond).

(18) (a) Pimentel, G. C. *J. Chem. Phys.* **1951**, *19*, 446−448. (b) Rundle, R. E. *Rec. Prog. Chem.* **1962**, *23*, 194−221. (c) Coulson, C. A. *J. Chem. Soc.* **1964**, *1964*, 1442−1454 ; Ref 1, p.278ff.

(19) In the present work, reference to "metallic" character of 3c/4e long-bonding should not be taken to imply literal *equivalence* to the bulk metallic limit. Rather, the terminology identifies this semi-localized bonding motif as the characteristic *alternative* to conventional 2c/2e molecular covalency (and its ω-type 3c/4e extension), which plays the role of a conceptual building block in an *Aufbau* picture of the limiting bulk phase. NBO-based methods for condensed phases [see Dunnington, B. D.; Schmidt, J. R. *J. Chem. Theory Comput.* **2012**, *8*, 1902−1911] may allow further aspects of the bulk metallic limit to be investigated.

(20) Herzberg, G. *Molecular Spectra and Molecular Structure. III. Electronic Spectra and Electronic Structure of Polyatomic Molecules*; Van Nostrand Reinhold: New York, 1966; p 427.

(21) For extensive discussion of electron-rich 3c/4e interactions from alternative MO-based perspective, see Munzarova, M. L.; Hoffmann, R. *J. Am. Chem. Soc.* **2002**, *124*, 4785−4795 **S1**.

(22) The closely related concept of "spin-paired diradical" long-bond resonance structures has been recognized by Harcourt and co-workers in the context of VB theory: Harcourt, R. D.; Hiigel, H. M. *J. Inorg. Nucl. Chem.* **1981**, *43*, 239−245. Skrezenek, F. L.; Harcourt, R. D. *J. Am. Chem. Soc.* **1984**, *106*, 3934−3936. Harcourt, R. D.; Styles, M. L. *J. Phys. Chem. A* **2003**, *107*, 3877−3883. Harcourt, R. D. *J. Phys. Chem. A.* **2011**, *115*, 6610−6616. Braida and Hiberty have similarly discussed long-bond structures in the context of "breathing orbital valence bond" (BOVB) calculations on trihalides: Braida, B.; Hiberty, P. C. *J. Phys. Chem. A.* **2008**, *112*, 13045−13052.

(23) Note that this circumstance points to an underlying inconsistency in *NBO 5.9* and preceding program versions which mandated an important notational change in the newly released *NBO 6.0* version (http://nbo6.chem.wisc.edu/new6_exc.htm; Ref 35). In former NBO versions, the "*" star label is used to designate both NBOs of low occupancy ("non-Lewis" BD*, RY*) and those of out-of-phase nodal character ("antibonding" σ*, π*, etc.), which normally causes no conflict in molecular ground-state species. However, these characteristics are clearly *in*consistent for the high-occupancy, out-of-phase long-bond NBOs, requiring a notational change to resolve the inconsistency. In the present work (as in *NBO 6.0*), we employ star labels exclusively to designate *out-of-phase orbital symmetry*, relying on context (or labelled output section) to distinguish high-occupancy donor (Lewis) and low-occupancy (non-Lewis) acceptor NBOs. At a more practical level, it should be noted that proper characterization of $\hat{\sigma}$ / $\hat{\sigma}$ * bonding formerly required $CHOOSE and $NRTSTR keylist work-arounds [see Weinhold, F.; Landis, C. R. *Discovering Chemistry with Natural Bond Orbitals*; Wiley: Upper Sadde River, NJ, 2012)], but is now handled seamlessly in *NBO 6.0*. NRT algorithms of *NBO 6.0* have also been significantly improved, but the numerical results of the present paper are obtained with the *NBO 5.9* version that is still most widely available in host electronic structure systems.

(24) Kutzelnigg, W. *Angew. Chem., Int. Ed.* **1984**, *23*, 272−295. Reed, A. E.; Weinhold, F. *J. Am. Chem. Soc.* **1986**, *108*, 3586−3593. Magnusson, E. *J. Am. Chem. Soc.* **1990**, *112*, 7940−7951. Suidan, L.; Badenhoop, J. K.; Glendening, E. D.; Weinhold, F. *J. Chem. Educ.* **1995**, *72*, 583−586.

(25) Hyman, H. H., Ed.; *Noble-Gas Compounds*; University of Chicago Press: Chicago, IL, 1963.

(26) Weinhold, F. *J. Comput. Chem.* **2012**, *33*, 2363−2379.

(27) Bader, R. F. W. *Atoms in Molecules: A Quantum Theory*; Oxford University Press: London, U.K., 1990; Matta, C. F.; Boyd, R. J., Eds.; *The Quantum Theory of Atoms in Molecules: From Solid State to DNA and Drug Design*; Wiley-VCH: Weinheim, Germany, 2007.

(28) Weinhold, F. *J. Comput. Chem.* **2012**, *33*, 2440−2449.

(29) Cadenbach, T.; Bollermann, T.; Gemel, C.; Fernandez, I.; von Hopffgarten, M.; Frenking, G.; Fischer, R. A. *Angew. Chem., Int. Ed.* **2008**, *47*, 9150−9154. Cadenbach, T.; Bollermann, T.; Gemel, C.; Tombul, M.; Fernandez, I.; von Hopffgarten, M.; Frenking, G.; Fischer, R. A. *J. Am. Chem. Soc.* **2009**, *131*, 16063−16077. Bollermann, T.; Cadenbach, T.; Gemel, C.; von Hopffgarten, M.; Frenking, G.; Fischer, R. A. *Chem. Eur.* **2010**, *16*, 13372−13384.

(30) Walsh, K. A. *Beryllium Chemistry and Processing*; ASM International: Materials Park, OH, 2009; Struzhkin, V. V.; Eremets, M. I.; Gan, W.; Mao, H. K.; Hemley, R. J. *Science* **2002**, *298*, 1213−1215. Yoshio, M.; Brodd, R. J.; Kozawa, A., *Lithium-Ion Batteries: Science and Technologies*; Springer: New York, 2009.

(31) Feng, J.; Hennig, R. G.; Ashcroft, N. W.; Hoffmann, R. *Nature* **2008**, *451*, 445−448.

(32) See, for example , Simons, J. *An Introduction to Theoretical Chemistry*; Cambridge University Press: Cambridge, U.K., 2003, Sec. 6.2.1.

(33) Note that NBO description of cyclic $(BeLi)_n$ differs qualitatively from that of seemingly analogous cyclic Li_n clusters such as D_{10h}-symmetric Li_{10} [see McAdon, M. H.; Goddard, W. A., III *Phys. Rev. Lett.* **1985**, *55*, 2563−2566. Lepetit, M.-B.; Malrieu, J.-P.; Spiegelmann, F. *Phys. Rev. B* **1990**, *41*, 8093−8106]. At B3LYP/6-311++G** level, the latter is aptly described by open-shell α, β spin-Kekulé structures, each with five alternating σ_{LiLi} spin-NBOs of conventional form.

(34) Note that the distinction between "molecular" and "metallic" bonding is far more fundamental than the (false) dichotomy between "covalent" and "ionic" bonding. The latter are merely opposite limits of a *continuous* range of 2c/2e bond polarities, whereas the former correspond to *disjoint* regions of the potential energy surface, separated by thermal activation barriers and characterized by *reversed* importance of Lewis-structural vs resonance-type donor−acceptor contributions to net binding.

(35) Glendening, E. D.; Landis, C. R.; Weinhold, F. *J. Comput. Chem.* (in press). DOI: 10.1002/jcc.23266.